Lawrence Berkeley National Laboratory
LBL Publications

Title

Enhancement of magnetic domain wall velocity via resonant dissipation of standing wave modes of domain wall structure with perpendicular magnetic anisotropy

Permalink

https://escholarship.org/uc/item/0mm9t6j1

Journal

Physical Review B, 110(21)

ISSN

2469-9950

Authors

Kim, Ganghwi
Jung, Dae-Han
Han, Hee-Sung
et al.

Publication Date

2024-12-01

DOI

10.1103/physrevb.110.214407

Peer reviewed

eScholarship.org Powered by the California Digital Library
University of California

Beyond Walker Breakdown through the Resonant Dissipation: Dramatic Enhancement of Magnetic Domain Wall Velocity via Resonant Excitation of Standing Wave Modes of Domain Wall Structure

Ganghwi Kim[1,*], Dae-Han Jung[1], Hee-Sung Han[2], Myeonghwan Kang[1], Suyeong Jeong[1], Younggun Park[3], Mi-Young Im[4], and Ki-Suk Lee[1,3,†]

[1]*School of Materials Science and Engineering, Ulsan National Institute of Science Technology (UNIST), Ulsan 44919, Republic of Korea*

[2]*Department of Materials Science and Engineering, Korea National University of Transportation, Chungju 27469 Republic of Korea.*

[3]*Graduate School of Semiconductor Materials and Devices Engineering, Ulsan National Institute of Science and Technology (UNIST), Ulsan 44919, Republic of Korea*

[4]*Center for X-ray Optics, Lawrence Berkeley National Laboratory, Berkeley, California 94720, USA*

Abstract

The dynamic behaviors of magnetic domain walls have significant implications for developing advanced spintronic devices. In this study, we investigate the intriguing resonance phenomenon within the magnetic domain wall structure and its profound influence on dynamic motion, focusing on the dissipation mechanism. By applying a static external magnetic field, we observe a remarkable amplification of domain wall velocity through the

resonant excitations of the flexure modes, surpassing the limitations of the conventional one-dimensional model. To quantify this enhancement, we establish a robust relationship between the time-averaged velocity of the DW motion and the time-averaged energy dissipation via the flexure-mode excitations by introducing a novel parameter - the distortion variation rate. Our findings provide crucial insights into the underlying mechanisms governing domain wall dynamics while paving the way for developing and optimizing next-generation spintronic devices boasting unparalleled speed and efficiency.

Receipt date: 23 February 2024

PACS number(s): 75.60.Ch, 75.78.Cd, 75.70.Ak, 05.10.−a

I. INTRODUCTION

The dynamics of magnetic domain walls (DWs) have been the subject of extensive study [1-3], driven by their potential applications in emerging spintronic information memory and processing devices [4-6]. Walker's pioneering work [7], based on the Landau-Lifshitz-Gilbert (LLG) equation, has significantly contributed to our understanding of DW motion, yielding the well-known Walker solution for one-dimensional (1D) models [8,9]. However, challenges emerge when attempting to apply the Walker solution to describe DW motion in confined systems, such as nanostrips, especially in cases of the regime beyond the Walker breakdown, where the DW structure undergoes precessional transformations during its motion. For instance, complicated DW motions involving inhomogeneous transverse and vortex DWs [10-12] and the enhancement of DW velocity through the excitation of the flexure modes of DWs in the film thickness [13,14] manifest substantial deviations from the rigid wall approximation of the 1D model. Notably, in cases involving a thick film with thickness exceeding the exchange length, the resonant excitation of flexure modes in the thickness direction gives rise to a standing wave akin to natural modes [15]. Analytical models have been developed to capture this phenomenon, accounting for the instantaneous DW profile during resonant excitation of flexure modes. However, persistent discrepancies in the enhancement of DW velocity between the analytical model and the simulation result remain, primarily attributed to the intricate dynamics of the resonant excitation of propagating DW [14].

Recently, the dynamics of the spin texture in the perpendicular magnetic anisotropy (PMA) thin film system have been a high-profile topic due to their applicational potentials [5,16-19]; therefore, understanding the DW dynamics is necessary. The DW in the PMA thin

film shows complicated motion compared to the 1D model, caused by different physical effects such as the Rashba effect [20], relativistic kinematics [21], vertical Bloch lines generated by the elongated system [22] or Dzyaloshinskii-Moriya interaction (DMI) [23-25]. In a manner analogous to the thick-film case, the flexure mode of the DW in PMA thin film induces intricate dynamics. However, it is worth noting that the nodes of standing waves of the flexure modes are oriented along the width direction rather than the thickness direction. This unique width-directional flexure mode has received limited attention in terms of theoretical and experimental research.

In this paper, we introduce a novel approach rooted in energy dissipation to comprehensively elucidate the dramatic enhancement of DW velocity observed during width-directional flexure mode resonance in an ultrathin film nanostrip system with PMA. The resonance, characterized by a substantial amplification of the standing wave modes in the DW's internal structure, induces pronounced oscillations that drive the DW back and forth within its position. Consequently, it exerts an indirect influence on the DW velocity through energy dissipation, leading to a significant enhancement from the predictions of the 1D Walker model. In our approach, we streamline the intricate dynamics of the DW by focusing on energy dissipation resulting from the resonant excitation of the DW flexure mode rather than considering the instantaneous dynamics of the DW structure. This approach enables a highly precise estimation of DW velocity.

II. MICROMAGNETIC SIMULATIONS

To investigate the effect of the resonance of the width-directional flexure mode on the DW velocity in PMA using micromagnetic simulations, we adopt a 106-nm-wide nanostrip with a thickness of 0.6 nm and a length of 1000 nm as depicted in Fig. 1. The PMA system employs typical materials parameters, mimicking a Pt/Co/Pt structure with a Co-monolayer thickness of 0.6 nm. These parameters include exchange constant (A) of 16 pJ/m, 1st order uniaxial anisotropy constant (K_u) of 1280 kA/m with an easy axis oriented along the film-thickness direction (z direction), saturation magnetization (M_s) of 1130 kA/m [26,27]. The exchange length is $\sqrt{A/(\mu_0 M_s^2)} \approx$ 3.16 nm, necessitating a mesh size of 2 × 2 × 0.6 nm^3, suitable for finite difference method numerical calculations. The dynamic evolution of the magnetization structure is deduced by solving the LLG equation [28] for each mesh. To emphasize DW resonances, a low damping parameter ($\alpha = 0.01$) is chosen.

The initial state is established with $+z$ and $-z$ magnetic domains on the left and right halves of the nanostrip, with the Bloch DW magnetized in the $+y$ direction between the two domains. To induce motion of the Bloch DW toward the $+x$ direction, a uniform static magnetic field ranging from H = 10 mT to 250 mT in the $+z$ direction is applied to the nanostrip. At the end of each time step, the entire magnetization structure is shifted slightly along the x direction to relocate the DW onto the system's center to implement an infinite strip [29,30]. The calculations are performed using the open-source micromagnetic simulation framework OOMMF [31].

A. Domain wall propagation model in a monolayer PMA nanostrip system

In the 1D Walker model of DW motion, the DW structure and its dynamics are characterized by the DW position $q_{1D}(t)$ with $m_z=0$ along the x axis and the time-varying azimuth angle $\phi_{1D}(t)$ of the magnetization vector ($\boldsymbol{m}$) at the DW position [7]. In a monolayer PMA nanostrip system with a width of L, the spatial variation of ϕ and q along the width direction ($\boldsymbol{y}$) is illustrated in Fig 1. Here, $q(y,t)$, represents the x position of the DW ($m_z=0$) along the width direction, and $\phi(y,t)$, denotes the azimuth angle of $\boldsymbol{m}$ over the q profile. The DW displacement is determined by the spatial average value of $q(y,t)$:

$$\dot{q}(t)=\frac{\int q(y,t)\,dy}{\int dy}=\frac{1}{L}\int q(y,t)\,dy, \quad (1)$$

where $\int dy=L$ for our nanostrip system. Consequently, the DW velocity can be obtained from the time derivative of the spatial-averaged DW displacement, $\ddot{q}(t)=d\dot{q}(t)/dt$. When the motion is periodic or steady, one can calculate the time-averaged value of the DW velocity:

$$\langle\dot{q}\rangle=\frac{\int \ddot{q}(t)\,dt}{\int dt}. \quad (2)$$

Similarly, the spatial-averaged and the time-averaged $\phi(y,t)$ can be defined as

$$\dot{\phi}(t)=\frac{1}{L}\int \phi(y,t)\,dy, \quad (3)$$

$$\langle\ddot{\phi}\rangle=\frac{\int \dddot{\phi}(t)\,dt}{\int dt}, \quad (4)$$

where $\ddot{\phi}(t)=d\dot{\phi}(t)/dt$.

B. Domain wall flexure mode excitation during domain wall propagation

Under a small perpendicular external magnetic field, the DW exhibits steady motion with a constant angle ϕ_{1D} and a constant velocity $\dot{q}_{1D}$ proportional to the field strength H. When the external magnetic field surpasses a specific threshold, known as the Walker field [7,8,32], the solution of the 1D Walker model reveals that the azimuth angle $\phi_{1D}(t)$ undergoes precession. Consequently, the DW position $q_{1D}(t)$ oscillates periodically back and forth with the frequency of $\sin(2\phi_{1D})$, leading to a significant reduction in the time-averaged velocity, $\langle \dot{q}_{1D} \rangle$, which is also proportional to the strength of the perpendicular external magnetic field H [3]:

$$\langle \dot{q}_{1D} \rangle = |\gamma| \Delta \frac{\alpha}{1+\alpha^2} H. \quad (5)$$

Here, $\gamma = -¿1.76 \times 10^{11}$ rad s^{-1} T^{-1} is the electron's gyromagnetic ratio, and $\Delta = \sqrt{A/(K_u - \mu_0 M_s^2/2)}$ is the static DW width. This equation is derived within the limits of the 1D model assuming a short length of the DW, which variation along the *y*-direction can be ignored, but it also matches quite well with longer DWs.

Figures 2(a) and (b) illustrate a comparison between numerical simulation results of DW motion in a monolayer PMA nanostrip system (dotted red lines) and the 1D Walker model solution (solid black lines) under H = 94 mT and 47 mT, respectively. For H = 94 mT, the simulation result is close to the Walker model, since, as shown in Fig. 2(c), the DW shape does not vary along the *y*-direction like the 1D model. However, for H = 47 mT, the DW motion in numerical results deviates dramatically from the model due to the excitation of the DW flexure mode during propagation, as evidenced by its distortion in Fig. 2(d).

C. Resonance of the domain wall flexure mode and the velocity enhancement

To quantify the degree of DW structural distortion in a monolayer PMA nanostrip system, the variances of $q(y,t)$ and $\phi(y,t)$ with respect to y are introduced as:

$$\mathrm{Var}(\tilde{q}) = \frac{1}{L}\int \left[\tilde{q}(y,t) - \bar{\tilde{q}}(t)\right]^2 dy, \quad (6a)$$

$$\mathrm{Var}(\phi) = \frac{1}{L}\int \left[\phi(y,t) - \bar{\phi}(t)\right]^2 dy, \quad (6b)$$

where $\tilde{q} = q/\Delta$, represents the dimensionless displacement normalized by the domain wall width Δ. The DW width may vary during the dynamic motion of the DW [3,10], but in this paper, it is considered as a constant for simplification [33].

Figure 3(a) illustrates the variation of the DW under H = 47 mT over a single period of the azimuthal angle precession (~ 0.76 ns). The variations of $\tilde{q}$ and ϕ occur alternately, resembling trigonometric functions with a phase difference of π. Snapshot images in Fig. 3(a) showing the magnetization configuration, along with $\tilde{q}$ and ϕ profiles of DW, clearly show that the sinusoidal DW flexure mode is resonantly excited at H = 47 mT and its frequency, 2.63 GHz, is the same as that of $\sin(2\bar{\phi})$. Notably, variances of both the displacement and the azimuth angle exhibit the standing-wave form with the same node locations, but their phase difference is $\pi/2$.

Figure 3(b) demonstrates diverse resonant excitations of DW flexure modes, accompanying a significant enhancement of the time-averaged DW velocity, $\langle \dot{\bar{q}} \rangle$, compared to that of the 1D model, $\langle \dot{q}_{1D} \rangle$. As depicted in the insets, in general, the wavelength of the sinusoidal profiles of the DW flexure modes is quantized, decreasing with the field strength *H,* but it is often not. For a more detailed interpretation, an analytic model for the curve DW should be introduced.

III. ANALYSIS OF DOMAIN WALL RESONANCE DISSIPATION

A. Normal modes of the domain wall flexure mode

In a monolayer PMA nanostrip system with a width of L, the magnetization in the DW follows the open-end boundary conditions [3] at the edge of the nanostrip width, which are

$$\left.\frac{\partial\theta}{\partial y}\right|_{y=0,L}=0,\ \left.\frac{\partial\phi}{\partial y}\right|_{y=0,L}=0, \quad (7)$$

where θ and ϕ are the polar and azimuth angles of the magnetization vector at $q(y,t)$, respectively. Based on the boundary conditions, the normal modes of $\tilde{q}$ and ϕ can be expressed as the set of generalized coordinates $\left(\tilde{q}_0,\widetilde{Q}_1,\widetilde{Q}_2,\cdots,\phi_0,\Phi_1,\Phi_2,\cdots\right)$, where

$$\tilde{q}_n(y,t)=\widetilde{Q}_n(t)\cos\left(\frac{n\pi y}{L}\right),\quad (8a)$$

$$\phi_n(y,t)=\Phi_n(t)\cos\left(\frac{n\pi y}{L}\right), \quad (8b)$$

with nonzero positive integer n. The DW position fluctuation $\tilde{q}_n$ and the angle twist ϕ_n with same n values compose a set of DW normal mode that $\widetilde{Q}_n(t)$ and $\Phi_n(t)$ are alternatively occur as mentioned in section II-C. Natural frequencies of $\widetilde{Q}_n(t)$ and $\Phi_n(t)$ are $\omega_n=n^2\omega_0$ where $\omega_0=(2A|\gamma|/M_s)\cdot(\pi/L)^2$ and their phase difference are $\pi/2$ for any n (see Appendix). Hence, as depicted in Fig. 4, $\tilde{q}(y,t)$ and $\phi(y,t)$ can be represented as the summation of the normal modes through Fourier cosine series [14,15]:

$\tilde{q}(y,t)=\tilde{q}_0(t)+\sum_{n=1}\tilde{q}_n(y,t)$, $\phi(y,t)=\phi_0(t)+\sum_{n=1}\phi_n(y,t)$, (9a) (9b) where $\tilde{q}_0(t)$ and $\phi_0(t)$ correspond to the 1D model satisfying the relations of Eqs. (A9) and (A10) in Appendix. For the given PMA system with L = 106 nm, $\omega_0/2\pi=0.697$ GHz, and thus the DW flexure mode excited at H = 47 mT whose frequency is 2.63 GHz corresponds to the $n=2$ mode with a frequency of $4\omega_0/2\pi$. Consequently, the value of $\widetilde{Q}_2$ and Φ_2 are much larger than others, as shown in the discrete Fourier transform results of $\tilde{q}(y,t)$ in Fig. 4(a) and $\phi(y,t)$ in Fig. 4(b).

Considering that the primary resonant frequency of the DW flexure mode aligns with twice the precession frequency of the DW azimuth angle $\dot{\phi}(t)$, the excited normal mode of the DW flexure mode primarily synchronizes with the second harmonic of DW magnetization precession. Analogous to the Larmor precession, the magnetization at the DW exhibits precessional motion under external field H, with a frequency proportional to the strength of H:

$f_p=\gamma_{DW}H$, (10) where the $\gamma_{DW}=28.51$ GHz T^{-1}. At H = 47 mT, $f_p=1.34$ GHz, and twice this precessional frequency, $2f_p=2.68$ GHz, align closely with the frequency of the second DW flexure mode $n=2$, $4\omega_0/2\pi$. This behavior is attributed to the DW acting as a parametric oscillator [13-15], driven by an in-plane stray field. The visualized result of fast Fourier transform (FFT) in Fig. 5(a) clearly illustrates this phenomenon. Since all $n\neq 0$ normal modes expressed as Eq. (9) have their antinodes on y = 0, the Fourier transform of the deviation of the DW azimuth angle at $y=0$ from its spatial-averaged value $\dot{\phi}(t)$ displays all excited modes except $\phi_0(t)$ as in Fig 5(a). Orange points signify intense resonance of modes with frequencies equivalent to x-coordinate values. The main diagonal line corresponds to the

primary excitation of the flexure modes, encompassing both resonance and off-resonance with $f = 2\gamma_{DW} H$. Resonant excitations manifest at the crossing point of the main diagonal line and the horizontal lines representing the natural frequencies of normal modes, $f_n = (n^2 \omega_0)/2\pi$. The nonlinear nature of the flexure mode excitation is characterized by mode splitting through the 4-magnon-scattering [34] at near H = 54,118, 184, 220, and 240 mT as well as higher harmonic resonant excitations. The sum of the FFT power in Fig. 5(b) demonstrates that the resonant excitation of the flexure mode leads to a significant enhancement in velocity.

B. Energy dissipation through domain wall flexure mode resonance

The relationship between DW flexure mode resonance and its velocity is elucidated by examining the energy dissipation in field-driven DW dynamics. Upon the application of a magnetic field, the Zeeman energy of the domain aligned parallel to the field decrease, whereas that of the domain aligned antiparallel to the field increases. To minimize the energy of the entire system, the domain aligned in parallel expands, causing the DW to move towards the domain aligned antiparallel to the field. Notably, the applied field, surpassing the Walker field of the DW, induces a back-and-forth motion of the DW. Consequently, the energy of the system does not decrease directly; instead, it diminishes through dissipation arising from the reciprocating motion of the DW. As a result, the time-averaged DW position $\langle \dot{q} \rangle$ gradually shifts towards where the domain is aligned antiparallel to the applied field, leading to a decrease in the Zeeman energy of the entire system due to DW dynamic dissipation.

Energy dissipation caused by the DW flexure mode excitation can be quantified using the Rayleigh dissipation function. The areal density of the DW Rayleigh dissipation function due to DW dynamics can be written as [35]

$$F=\frac{\alpha M_s}{|\gamma|}\left(\frac{\dot{q}^2}{\Delta}+\Delta\dot{\phi}^2\right). \quad (11)$$

The DW thickness is variable, but since $|\dot{\Delta}| \ll |\dot{q}|$ [33], treat Δ as a constant. From the Fourier cosine series of $\tilde{q}(y,t)$ and $\phi(y,t)$ in (8) and (9), and exploiting the orthogonality of trigonometric functions, the areal density of the Rayleigh dissipation function can be reformulated as

$$F=\frac{\alpha M_s \Delta}{2|\gamma|}\left[2\dot{\tilde{q}}_0^2+2\dot{\phi}_0^2+\sum_{n=1}\left(\dot{\tilde{Q}}_n^2+\dot{\Phi}_n^2\right)\right]. \quad (12)$$

Suppose a DW moved sufficiently far distance during a long enough time. The energy loss caused by that displacement is approximately equivalent to the decrease in Zeeman energy, specifically, $2M_s H\tilde{q}_0$ per unit area of DW. Neglecting the fluctuation of $\tilde{q}(y,t)$, the average DW energy loss per unit time and area is

$$\langle\dot{\sigma}_{loss}\rangle=2M_s H\Delta\langle\dot{\tilde{q}}_0\rangle. \quad (13)$$

Meanwhile, the rate of energy loss due to damping is twice the time-averaged Rayleigh dissipation function,

$$\langle\dot{\sigma}_{loss}\rangle=2\langle F\rangle=\frac{\alpha M_s \Delta}{|\gamma|}\left(2\langle\dot{\tilde{q}}_0^2\rangle+2\langle\dot{\phi}_0^2\rangle+D\right), \quad (14)$$

where D corresponds to the quantity of total distortion variation rate that is defined as

$$D\equiv\sum_{n=1}D_n=\sum_{n=1}\left(\langle\dot{\tilde{Q}}_n^2\rangle+\langle\dot{\Phi}_n^2\rangle\right) \quad (15)$$

using generalized coordinates. D is the same as the velocity of the DW in $2n$-dimensional phase space and can represent the amount of energy dissipation originated by DW resonance only. Figure 6(a) displays the field strength dependency of D_n.

The variation rate D_n tends to form peaks with larger amplitude for high n values since the resonance frequency is proportional to n^2.

C. Velocity enhancement of the domain wall through the resonant dissipation

The instantaneous DW velocity is determined by the time derivative of the spatial average value of the DW displacement, denoted as $\dot{q}(t)$ in Eq.(1). The $\dot{q}(t)$ is obtained from the summation of integrals over all normal modes, as defined in Eq. (9a). Notably, most mode integrations cancel out, excepting only the mode with $n = 0$. Consequently, the DW velocity $\dot{\bar{q}}(t) = \dot{q}_0(t)$ and its time-averaged value $\langle \dot{\bar{q}} \rangle = \langle \dot{q}_0 \rangle$.

Given that $\tilde{q}_0(t)$ and $\phi_0(t)$ satisfy the 1D model relations [7],

$$\dot{\phi}_0 = |\gamma| H - \alpha \dot{\tilde{q}}_0, \tag{16}$$

Equations (13) and (14) can be written in terms of $\langle \dot{\tilde{q}}_0^2 \rangle$ and $\langle \dot{\tilde{q}}_0 \rangle$:

$$(1+\alpha^2)\langle \dot{\tilde{q}}_0^2 \rangle - \frac{1+2\alpha^2}{\alpha}|\gamma| H \langle \dot{\tilde{q}}_0 \rangle + (|\gamma| H)^2 + \frac{D}{2} = 0. \tag{17}$$

For high enough field, the first term of (17) can be negligible, hence it yields the time-averaged velocity of the DW in the form of D and H:

$$\langle \dot{\bar{q}} \rangle = \langle \dot{q}_0 \rangle = \Delta \frac{\alpha}{1+2\alpha^2}\left(|\gamma| H + \frac{D}{2|\gamma| H} \right) \\ \lesssim \langle \dot{q}_{1D} \rangle + \frac{\alpha \Delta}{1+2\alpha^2}\frac{D}{2|\gamma| H}. \tag{18}$$

In the low damping system, Eq. (18) converges to the 1D model given by Eq. (5) when $D = 0$.

The parameter D serves as a predictive indicator for the DW velocity, as demonstrated in Fig. 6(b). The black line illustrates the anticipated velocity increment, corresponding to the second term on the right side of Eq. (18). In comparison, the orange line depicts the DW velocity increment, $\langle \dot{q}_0 \rangle - \langle \dot{q}_{1D} \rangle$ resulted from numerical simulations. The predicted value aligns well with the numerical result. Since the eigenfrequency of flexure mode is proportional to the square of mode number n^2, high D_n value is shown when high flexure mode emerges. The distortion variation rate affects on the DW velocity increment as in the form of D/H in Eq. (18), therefore, a high D does not necessarily imply a higher velocity increment. For instance, the Dvalue under 184 mT is about ten times that under 12 mT, but velocity increment is similar.

In the higher H range, where excitation of the 4$^{\text{th}}$ flexure mode becomes prominent, a noticeable discrepancy arises. This indicates the presence of an additional energy dissipation channel, beyond the consideration of flexure modes alone. This channel corresponds to spin waves. In principle, the DW flexure mode can emit spin waves to the adjacent domains when the excited spin waves attain a sufficiently high frequency to overcome the forbidden band in the domain [19]. In our system, spin waves commence emission at the 4$^{\text{th}}$ flexure mode, but this phenomenon is not explicitly addressed in the current study.

IV. CONCLUSIONS

We have identified the energy dissipation resulting from DW flexure mode resonance as the primary factor behind the DW velocity increment. Treating the DW resonance as a

parametric oscillator reveals its vibration in various shapes, decomposed into standing waves. This oscillation induces magnetization structure deformation, resulting in the energy dissipation of system which is the main driving force of the long-term DW motion. The energy-dissipation rate can be quantified through the DW distortion variation rate, D. Moreover, for higher resonant modes of the DW flexure modes, an additional dissipation channel emerges - spin wave emission from the DW - further enhancing the DW velocity. This study provides an elegant interpretation of the DW motion's periodic dynamics by considering the time-averaged energy dissipation of DW dynamics. These insights gained from this research extend to other magnetic systems, such as magnetic skyrmions, bubbles, and magnetic vortices.

ACKNOWLEDGEMENTS

This work was supported by the NRF grant funded by the Korea government (MSIT) (RS-2023-00217968 and 2020M3F3A2A03082987), the 2023 Research Fund (1.230013.01 and 1.230063.01) of UNIST (Ulsan National Institute of Science and Technology), and the Korea Institute for Advancement of Technology (KIAT) grant funded by the Korea Government (MOTIE) (P0023703, HRD Program for Industrial Innovation). M.-Y. I. acknowledges support from the U.S. Department of Energy (DE-AC02-05CH11231).

APPENDIX: SOLUTION OF EULER-LAGRANGE EQUATION ABOUT DOMAIN WALL

The starting point of understanding the DW dynamics is knowing its potential energy. Suppose a thin film magnetic system long in the *x*-direction with PMA. The DW is formed along the *y*-axis, and its length is long enough that it cannot be treated as a 1D DW. Form the boundary condition $\theta(\pm\infty)=(\pi,0)$, the ansatz of the DW structure is derived as [33]

$$\phi(x)=\text{const},\ \theta(x)=2\arctan\exp\left[\frac{(x-q)}{\Delta}\right], \tag{A1}$$

where q is the center of the DW. The local energy density of the DW system is [3]

$$w_{\text{flat}}(\theta,\phi)=A\left[\left(\frac{\partial\theta}{\partial x}\right)^2+\left(\sin\theta\frac{\partial\phi}{\partial y}\right)^2\right]+K_u\sin^2\theta + \frac{H_{DW}M_s}{2}\sin^2\theta\sin^2\phi-M_sH\cos\theta, \tag{A2}$$

where H_{DW} is the energy difference between the Bloch wall and the Néel wall. Note that polar angle θ does not vary along *y* direction since the DW is flat. The areal density of a flat DW potential energy is derived as

$$\sigma_{\text{flat}}(q,\phi)=\sigma_0+2A\Delta\left(\frac{\partial\phi}{\partial y}\right)^2+H_{DW}M_s\Delta\sin^2\phi-2M_sHq, \tag{A3}$$

by integrating (A3) using ansatz (A1) and (A2). $\sigma_0=4\sqrt{AK_u}$ is areal energy density of the Bloch wall. Now, suppose that the DW is slightly curved. The potential energy of the elongated DW is increased as the amount of extended length [3]. Hence

$$\sigma(q,\phi)=\sigma_{\text{flat}}(q,\phi)\sqrt{1+\left(\frac{\partial q}{\partial y}\right)^2}$$
$$\approx \sigma_0\left[1+\frac{1}{2}\left(\frac{\partial q}{\partial y}\right)^2\right]+2A\Delta\left(\frac{\partial \phi}{\partial y}\right)^2+H_{DW}M_s\Delta\sin^2\phi-2M_sHq. \quad \text{(A5)}$$

Since the given system is ultrathin, the variance of any energy term and variables along the z-direction is negligible.

The density of the Lagrangian of a magnetic spin system is [35]

$$L_{\text{d}}(\theta,\phi)=\frac{-M_s}{|\gamma|}\dot{\phi}\cos\theta-w(\theta,\phi). \quad \text{(A6)}$$

The first term on the right side is about the Berry phase of spins [36], and the second term $w(\theta,\phi)$ is the potential energy density of the magnetic structure. Using (A1), (A2) and (A5), the areal density of DW Lagrangian is

$$L_{\text{ad}}(q,\phi)=\frac{-2M_s}{|\gamma|}\dot{\phi}q-\sigma(q,\phi)$$
$$¿-\frac{2M_s}{|\gamma|}\dot{\phi}q-\frac{\sigma_0}{2}\left(\frac{\partial q}{\partial y}\right)^2-2A\Delta\left(\frac{\partial \phi}{\partial y}\right)^2-H_{DW}M_s\Delta\sin^2\phi+2M_sHq. \quad \text{(A7)}$$

Constant σ_0 is omitted. Hence L_{ad} is a functional about DW position $q(y,t)$ and DW azimuth angle $\phi(y,t)$. Similar to the areal density of the DW Rayleigh dissipation function in Eq. (12), Lagrangian also can be transformed into a form for the set of generalized coordinates $\left(\tilde{q}_0,\widetilde{Q}_1,\widetilde{Q}_2,\cdots,\phi_0,\Phi_1,\Phi_2,\cdots\right)$

based on (8) and (9):

$$L=\frac{2M_s\Delta}{|\gamma|}\left[-2\dot{\phi}_0\tilde{q}_0+2|\gamma|H\tilde{q}_0-\frac{\gamma H_{DW}}{L}\int_0^L\sin^2\phi(y)dy\right.$$
$$\left.-\sum_{n=1}\left(\dot{\Phi}_n\tilde{Q}_n+\frac{1}{2}n^2\omega_0\tilde{Q}_n^2+\frac{1}{2}n^2\omega_0\Phi_n^2\right)\right], \quad \text{where } \omega_0\equiv(2A|\gamma|/M_s)\cdot(\pi/L)^2. \tag{A8}$$

Solving the Euler-Lagrange equation about Eq. (12) and (A8), one can drive the set of equations of motion. For $n=0$, $\frac{d}{dt}\frac{\partial L}{\partial\dot{\tilde{q}}_0}-\frac{\partial L}{\partial\tilde{q}_0}+\frac{\partial F}{\partial\dot{\tilde{q}}_0}=2\dot{\phi}_0-2|\gamma|H+2\alpha\dot{\tilde{q}}_0=0$, (A9)

$\frac{d}{dt}\frac{\partial L}{\partial\dot{\phi}_0}-\frac{\partial L}{\partial\phi_0}+\frac{\partial F}{\partial\dot{\phi}_0}=-2\dot{\tilde{q}}_0+I_0+2\alpha\dot{\phi}_0=0$, (A10) where

$I_n=\frac{\gamma H_{DW}}{L}\int_0^L\sin 2\phi\cos\frac{n\pi y}{L}dy$. (A11) Equations (A9) and (A10) are the same results as the 1D DW model. In the case of 1D, time-averaged integral $\langle I_0\rangle$ is negligible when the Walker breakdown is occurred [8]. However, when the DW resonates, $n\neq 0$ terms emerge and $\langle I_0\rangle$ is no longer negligible.

For $n \neq 0$,

$$\frac{d}{dt}\frac{\partial L}{\partial \dot{\widetilde{Q}}_n}-\frac{\partial L}{\partial \widetilde{Q}_n}+\frac{\partial F}{\partial \dot{\widetilde{Q}}_n}=\dot{\Phi}_n+n^2\omega_0\widetilde{Q}_n+\alpha\dot{\widetilde{Q}}_n=0, \quad \text{(A12)}$$

$$\frac{d}{dt}\frac{\partial L}{\partial \dot{\Phi}_n}-\frac{\partial L}{\partial \Phi_n}+\frac{\partial F}{\partial \dot{\Phi}_n}=-\dot{\widetilde{Q}}_n+n^2\omega_0\Phi_n+I_n+\alpha\dot{\Phi}_n=0. \quad \text{(A13)}$$

Thus,

$$(1+\alpha^2)\dot{\Phi}_n=-n^2\omega_0(\widetilde{Q}_n+\alpha\Phi_n)-\alpha I_n, \quad \text{(A14)}$$

$$(1+\alpha^2)\dot{\widetilde{Q}}_n=n^2\omega_0(\Phi_n-\alpha\widetilde{Q}_n)-I_n. \quad \text{(A15)}$$

In polar coordinates,

$$\dot{r}_n=\frac{1}{(1+\alpha^2)}\left[-\alpha n^2\omega_0 r_n-(\sin\theta_n+\alpha\cos\theta_n)I_n\right], \quad \text{(A16)}$$

$$\dot{\theta}_n=\frac{1}{(1+\alpha^2)}\left[n^2\omega_0 r_n+(\alpha\sin\theta_n-\cos\theta_n)I_n\right], \quad \text{(A17)}$$

where

$$r_n=\sqrt{\widetilde{Q}_n^2+\Phi_n^2}, \quad \text{(A18)}$$

and $\theta_n=\arctan(\Phi_n)$. Ignoring I_n, Equations [(A12)-(A17)] draw a CCW spiral trajectory on $\Phi_n-\widetilde{Q}_n$ phase space with a stable fixed point at the origin. The radial velocity $\dot{r}_n$ is proportional to $\alpha n^2\omega_0 r_n/(1+\alpha^2)$, therefore the resonance decay ratio is proportional to the resonance amplitude r_n, damping of system $\alpha/(1+\alpha^2)$, and the square of the mode number n^2. The angular velocity $\dot{\theta}_n$ is proportional to $n^2\omega_0 r_n/(1+\alpha^2)$, hence the frequency of resonance mode is $n^2\omega_0/(1+\alpha^2)$. Here, stray field integral I_n acts as the external force that arouses the resonance and pushes the trajectory away from the origin against $\dot{r}_n$.

Figure 7(a) illustrates the stabilized trajectory of the DW in the $\Phi_n-\widetilde{Q}_n$ phase space under H = 47 mT field. The DW draws a large limit cycle rotating in the CCW direction on

the $\Phi_2 - \widetilde{Q}_2$phase space, but trajectories in the other $\Phi_n - \widetilde{Q}_n$ spaces are significantly smaller. In this condition, the limit cycle is drawn as a circle. This trajectory of DW in the $\Phi_n - \widetilde{Q}_n$ phase space is determined by mutual confrontation between dissipation and driven force I_n. In the phase space, distorted DW draws a spiral with angular frequency $n^2 \omega_0 / (1+\alpha^2)$, falling to the origin with a radial velocity proportional to $\alpha / (1+\alpha^2)$, but the resonance caused by I_n pushes the DW away from the origin. The scale of the trajectory can be quantified using its radius r_n that depicted in Fig. 7(b). The r_2 value that is relatively larger than other r_n and shows the uniform tendency proves the manifestation and stabilization of the n = 2 mode. The schematic diagrams of the DW during the 2-period of the limit cycle are enumerated in Fig. 7(c). The DW alternatively changes its shape from the flexure states $\left(\left|\widetilde{Q}_2\right| > 0\right)$ to the twisted angle states $\left(\left|\Phi_2\right| > 0\right)$.

REFERENCES

* ganghwi@unist.ac.kr

† Corresponding author, kisuk@unist.ac.kr

[1] J. C. Slonczewski, J. Appl. Phys. 44, 1759 (1973).

[2] A. Hubert and R. Schäfer, *Magnetic domains: the analysis of magnetic microstructures* (Springer, Berlin, 1998).

[3] A. P. Malozemoff and J. C. Slonczewski, *Magnetic domain walls in bubble materials* (Academic, New York, 1979).

[4] S. S. P. Parkin, M. Hayashi, and L. Thomas, Science 320, 190 (2008).

[5] S. F. Nafea, A. A. S. Dessouki, S. El-Rabaie, B. E. Elnaghi, Y. Ismail, and H. Mostafa, Integr. 65, 149 (2019).

[6] D. A. Allwood, G. Xiong, C. C. Faulkner, D. Atkinson, D. Petit, and R. P. Cowburn, Science 309, 1688 (2005).

[7] N. L. Schryer and L. R. Walker, J. Appl. Phys. 45, 5406 (1974).

[8] A. Mougin, M. Cormier, J. P. Adam, P. J. Metaxas, and J. Ferré, Europhys. Lett. 78, 57007 (2007).

[9] E. Martinez, S. Emori, N. Perez, L. Torres, and G. S. D. Beach, J. Appl. Phys. 115, 213909 (2014).

[10] O. A. Tretiakov, D. Clarke, G.-W. Chern, Y. B. Bazaliy, and O. Tchernyshyov, Phys. Rev. Lett. 100, 127204 (2008).

[11] S.-K. Kim, J.-Y. Lee, Y.-S. Choi, K. Y. Guslienko, and K.-S. Lee, Appl. Phys. Lett. 93, 052503 (2008).

[12] J.-Y. Lee, K.-S. Lee, S. Choi, K. Y. Guslienko, and S.-K. Kim, Phys. Rev. B 76, 184408 (2007).

[13] L. Thevenard, C. Gourdon, S. Haghgoo, J. P. Adam, H. J. v. Bardeleben, A. Lemaitre, W. Schoch, and A. Thiaville, Phys. Rev. B 83, 245211 (2011).

[14] C. Gourdon, L. Thevenard, S. Haghgoo, and A. Cebers, Phys. Rev. B 88, 014428 (2013).

[15] J. C. Slonczewski, J. Magn. Magn. Mater. 23, 305 (1981).

[16] B. Dieny and M. Chshiev, Rev. Mod. Phys. 89, 025008 (2017).

[17] D.-H. Jung, H.-S. Han, N. K. Kim, G. H. Kim, S. Y. Jeong, S. S. Lee, M. H. Kang, M.-Y. Im, and K.-S. Lee, Phys. Rev. B 104, L060408 (2021).

[18] H.-S. Han, S. S. Lee, S.-G. Je, M. H. Kang, H.-J. Ok, N. K. Kim, W. Chao, M.-Y. Im, and K.-S. Lee, ACS Appl. Nano Mater. 4, 9912 (2021).

[19] F. Garcia-Sanchez, P. Borys, R. Soucaille, J. P. Adam, R. L. Stamps, and J. V. Kim, Phys. Rev. Lett. 114, 247206 (2015).

[20] I. M. Miron, T. Moore, H. Szambolics, L. D. Buda-Prejbeanu, S. Auffret, B. Rodmacq, S. Pizzini, J. Vogel, M. Bonfim, and A. Schuhl, Nature materials 10, 419 (2011).

[21] L. Caretta, S.-H. Oh, T. Fakhrul, D.-K. Lee, B. H. Lee, S. K. Kim, C. A. Ross, K.-J. Lee, and G. S. Beach, Science 370, 1438 (2020).

[22] J. Hütner, T. Herranen, and L. Laurson, Phys. Rev. B 99, 174427 (2019).

[23] Y. Yoshimura, K.-J. Kim, T. Taniguchi, T. Tono, K. Ueda, R. Hiramatsu, T. Moriyama, K. Yamada, Y. Nakatani, and T. Ono, Nature Phys. 12, 157 (2016).

[24] V. Krizakova, J. P. Garcia, J. Vogel, N. Rougemaille, D. de Souza Chaves, S. Pizzini, and A. Thiaville, Phys. Rev. B 100, 214404 (2019).

[25] K. Yamada and Y. Nakatani, Appl. Phys. Express 8, 093004 (2015).

[26] A. Thiaville, S. Rohart, É. Jué, V. Cros, and A. Fert, Europhys. Lett. 100, 57002 (2012).

[27] P. J. Metaxas, J. P. Jamet, A. Mougin, M. Cormier, J. Ferré, V. Baltz, B. Rodmacq, B. Dieny, and R. L. Stamps, Phys. Rev. Lett. 99, 217208 (2007).

[28] L. Landau and E. Lifshitz, *On the theory of the dispersion of magnetic permeability in ferromagnetic bodies* (Pergamon, Oxford, 1992), Perspectives in Theoretical Physics.

[29] Y. Nakatani, A. Thiaville, and J. Miltat, Nat. Mater. 2, 521 (2003).

[30] A. Thiaville, Y. Nakatani, J. Miltat, and Y. Suzuki, Europhys. Lett. 69, 990 (2005).

[31] M. J. Donahue and D. G. Porter, *OOMMF user's guide, version 1.0* (National Institute of Standards and Technology, Gaithersburg, 1999).

[32] S. Glathe, R. Mattheis, and D. Berkov, Applied Physics Letters 93 (2008).

[33] J. C. Slonczewski, J. Appl. Phys. 45, 2705 (1974).

[34] S. Rajasekar and M. A. F. Sanjuan, *Nonlinear resonances* (Springer, Cham, 2016).

[35] B. Hillebrands and A. Thiaville, *Spin Dynamics in Confined Magnetic Structures III* (Springer, Berlin, 2006), Vol. 101.

[36] H.-B. Braun and D. Loss, Phys. Rev. B 53, 3237 (1996).

FIGURE CAPTIONS

FIG. 1. Schematic representation of the cobalt thin film nanowire and its magnetization structure. The nanowire is divided into two halves, with the left half magnetized in the $+z$ direction, and the right half in the $-z$ direction. A uniform magnetic field is applied in the $+z$ direction. The enlarged image illustrates the magnetization structure at the center of the system. The domain wall (DW) is defined along the line where $m_z = 0$. The initial position of the DW is denoted as $q(y, 0)$, and the displacement of the DW from the initial position at time t is represented as $q(y, t)$.The azimuth angle of the magnetization at $q(y, t)$ is defined as $\phi(y, t)$.

FIG. 2. The difference in domain wall (DW) dynamics under resonance. (a) and (b) depict the time dependence of the resonating DW displacement under the applied field H = 94 mT and 47 mT, respectively. The black solid line represents the result from numerical simulation, while the dotted red line corresponds to the 1D model approximation given by Eq. (5). (c) and (d) show the time-variance profile of the DW under H = 94 mT and 47 mT, respectively. Each dashed line shows the $q(y, t)$line at t = 0, 15, 30, and 45 ns.

FIG. 3. (a) The variation of the domain wall (DW) structure during a single period of dynamics under H = 47 mT. The Blue line represents the variance of $\tilde{q}(y, t) = q/\Delta$, and the red line shows the variance of $\phi(y, t)$, with respect to y. The black line indicates the cosine of the spatial average of the azimuth angles, $\bar{\phi}$. The images at the lower panel depict the magnetization structure at each extremum of the variances. (b) Field strength dependence of the time-averaged DW velocity. Each value is obtained by averaging over 20 ns after the system is stabilized. The black line is derived from the micromagnetic simulation, and the

blue line follows the 1D model given by Eq. (5). The gray colored area on the left indicates the region including not only the below Walker breakdown field but also the transient DW motion region, where the time-averaged DW velocity does not exhibit a proportional relationship with H. Insets in (b) depict schematics of the most severely bent DW profile at each velocity peak.

FIG. 4. Decomposition of the domain wall (DW) profile of (a) $\tilde{q}$ and (b) ϕ under H = 47 mT using a discrete Fourier transform. The amplitude of each term consists of the generalized coordinate $\left(\tilde{q}_0, \tilde{Q}_1, \tilde{Q}_2, \cdots, \phi_0, \Phi_1, \Phi_2, \cdots\right)$.

FIG. 5. Fast Fourier transformation (FFT) results for the domain wall (DW). (a) Field strength dependence of the time-domain FFT power of $\phi(0,t)-\phi_0(t)$. Four horizontal dashed lines indicate the frequency of the DW normal modes with n = 1, 2, 3, and 4, as illustrated in the boxes at the right. (b) The sum of FFT power.

FIG. 6. (a) Stacked graph of the time-averaged DW distortion variation rate D_n. The height of the graph depicts the total DW distortion variation rate $D=\Sigma D_n$. (b) The difference between the 1D model approximation of the time-averaged DW velocity and the micromagnetic simulation results. DW velocity is derived from the simulation in two ways: estimation using the total DW distortion rate D (black line) and direct calculation from the magnetization structure, $\langle\dot{q}_0\rangle-\langle\dot{q}_{1D}\rangle$. (orange line).

FIG. 7. The dynamics of the DW under H = 47 mT inside the $\tilde{Q}_n-\Phi_n$ phase space. (a) The trajectories of the DW inside the phase space after the dynamics of the DW is stabilized. (b)

Time dependence of the strength of the DW distortion $r_n=\sqrt{\widetilde{Q}_n^2+\Phi_n^2}$. (c) Snapshots of magnetization during two periods of motion inside the phase space. Each vertical line shows two periods that draw a single $n = 2$ limit cycle and emerge alternatively.

FIG. 1.

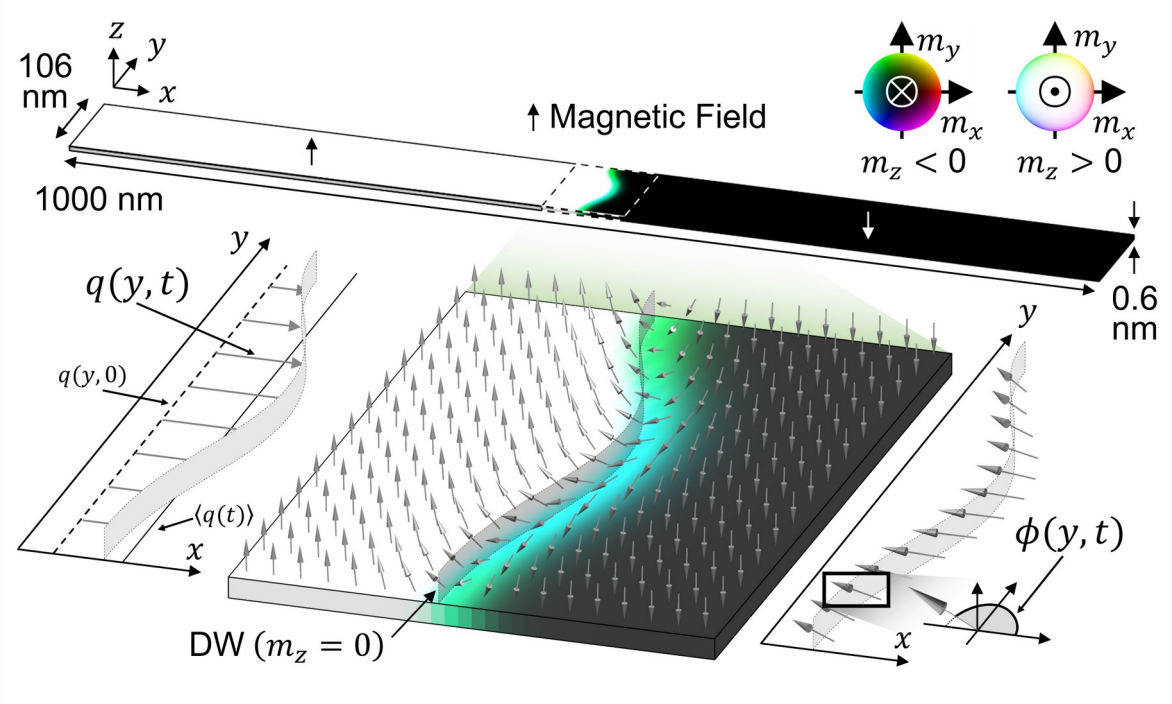
z
y
x
106 nm
1000 nm
Magnetic Field
m_y
m_x
$m_z < 0$
m_y
m_x
$m_z > 0$
0.6 nm
y
$q(y,t)$
$q(y,0)$
$\langle q(t) \rangle$
x
DW ($m_z = 0$)
y
$\phi(y,t)$
x

FIG. 2.

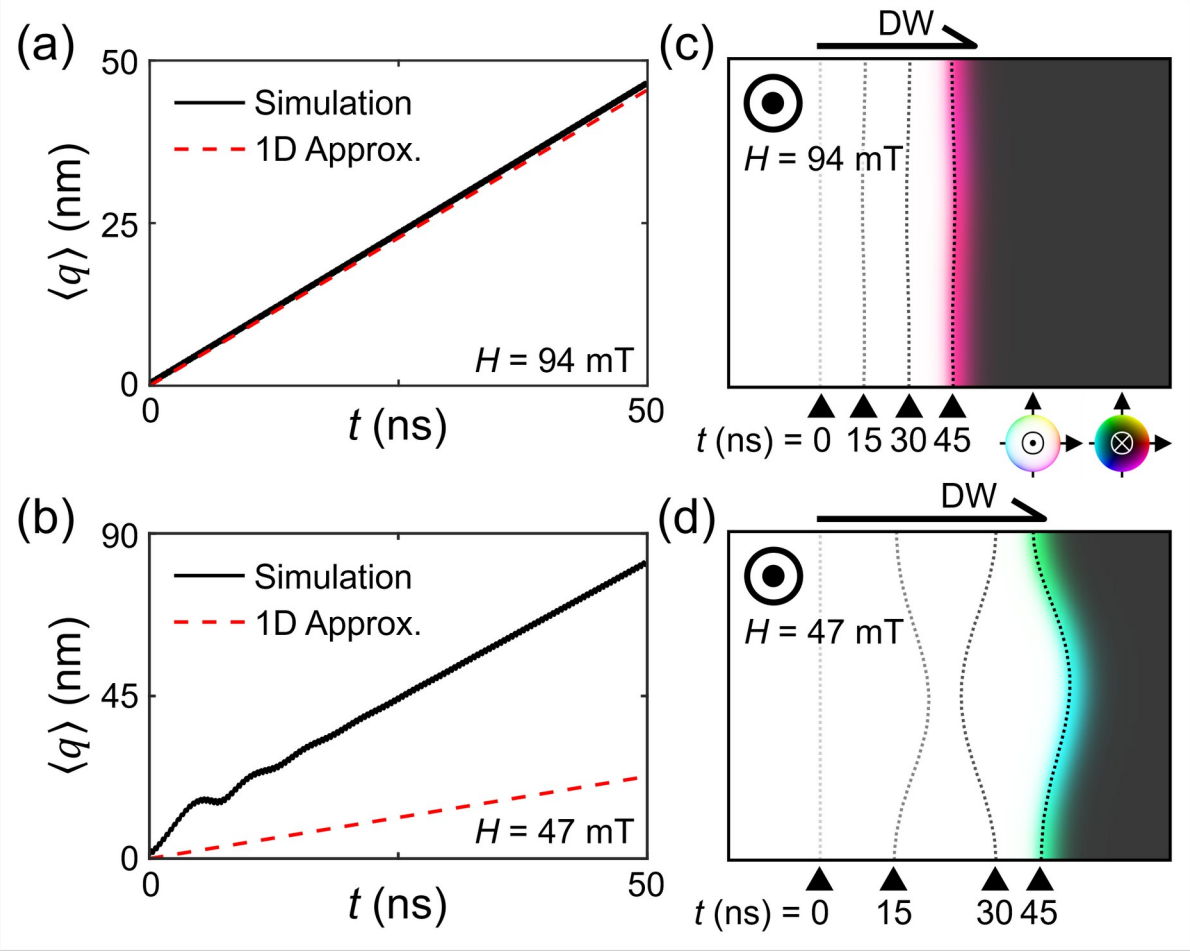
(a)
50
25
0
⟨q⟩ (nm)
Simulation
1D Approx.
H = 94 mT
0
50
t (ns)
(b)
90
45
0
⟨q⟩ (nm)
Simulation
1D Approx.
H = 47 mT
0
50
t (ns)
(c)
DW
H = 94 mT
t (ns) = 0 15 30 45
(d)
DW
H = 47 mT
t (ns) = 0 15 30 45

FIG. 3.

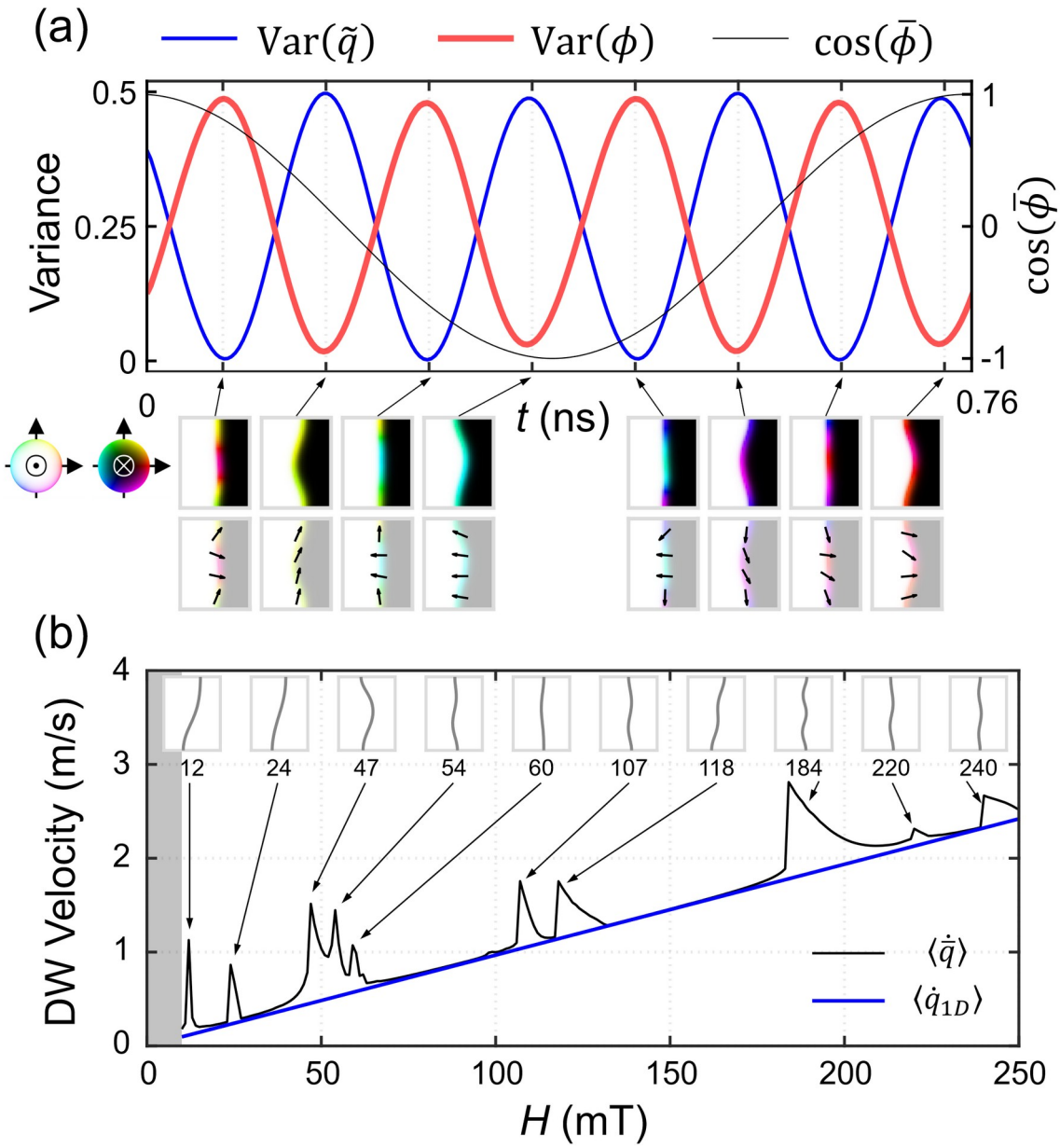
(a)
Var($\tilde{q}$)
Var(ϕ)
cos($\bar{\phi}$)
Variance
0.5
0.25
0
1
0
-1
cos($\bar{\phi}$)
0
t (ns)
0.76
(b)
DW Velocity (m/s)
4
3
2
1
0
12
24
47
54
60
107
118
184
220
240
$\langle\dot{\bar{q}}\rangle$
$\langle\dot{q}_{1D}\rangle$
0
50
100
150
200
250
H (mT)

FIG. 4.

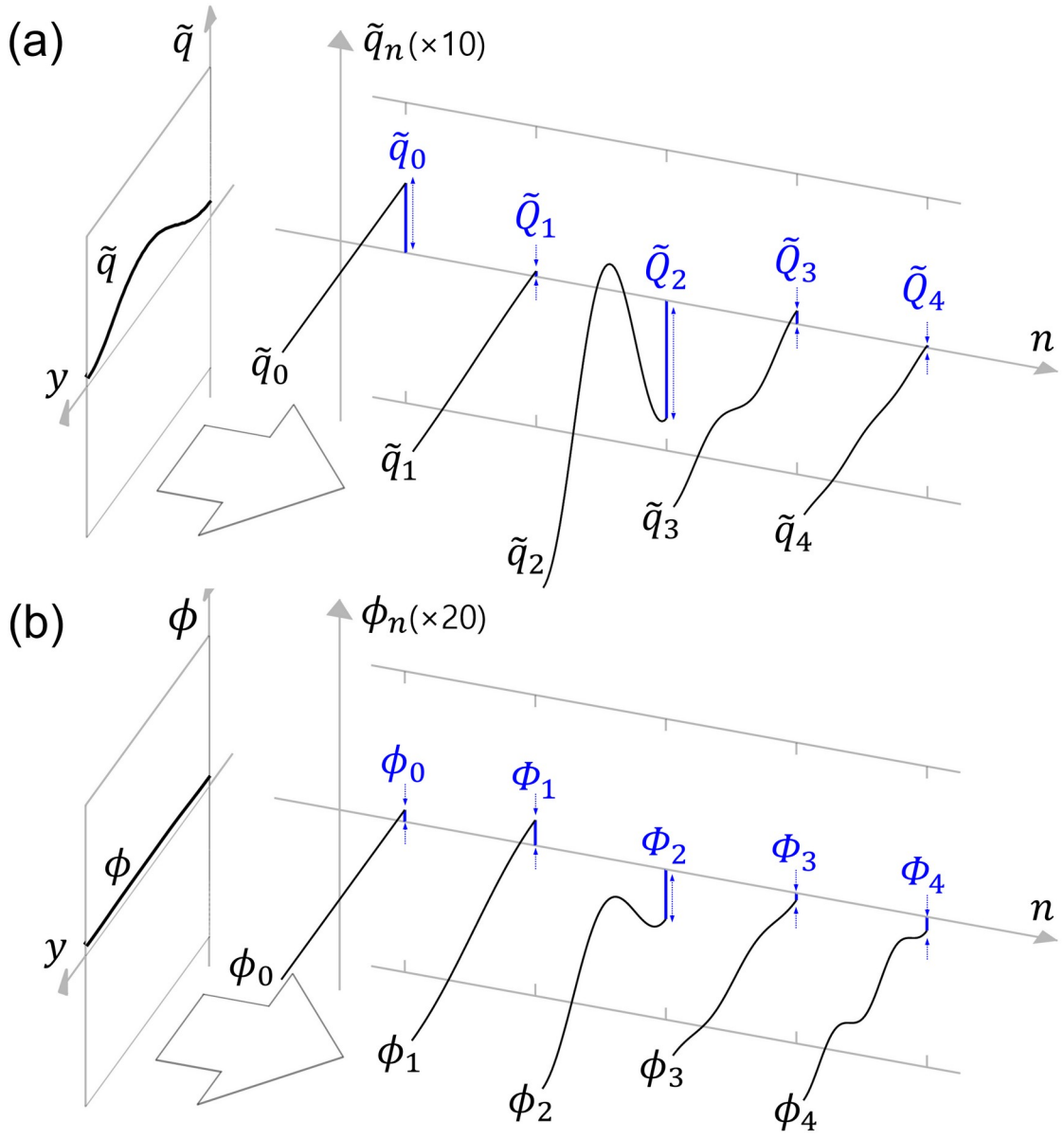
(a)
$\tilde{q}$
$\tilde{q}_n(\times 10)$
$\tilde{q}_0$
$\tilde{Q}_1$
$\tilde{Q}_2$
$\tilde{Q}_3$
$\tilde{Q}_4$
$\tilde{q}$
y
$\tilde{q}_0$
n
$\tilde{q}_1$
$\tilde{q}_2$
$\tilde{q}_3$
$\tilde{q}_4$
(b)
ϕ
$\phi_n(\times 20)$
ϕ_0
Φ_1
Φ_2
Φ_3
Φ_4
ϕ
y
ϕ_0
n
ϕ_1
ϕ_2
ϕ_3
ϕ_4

FIG. 5.

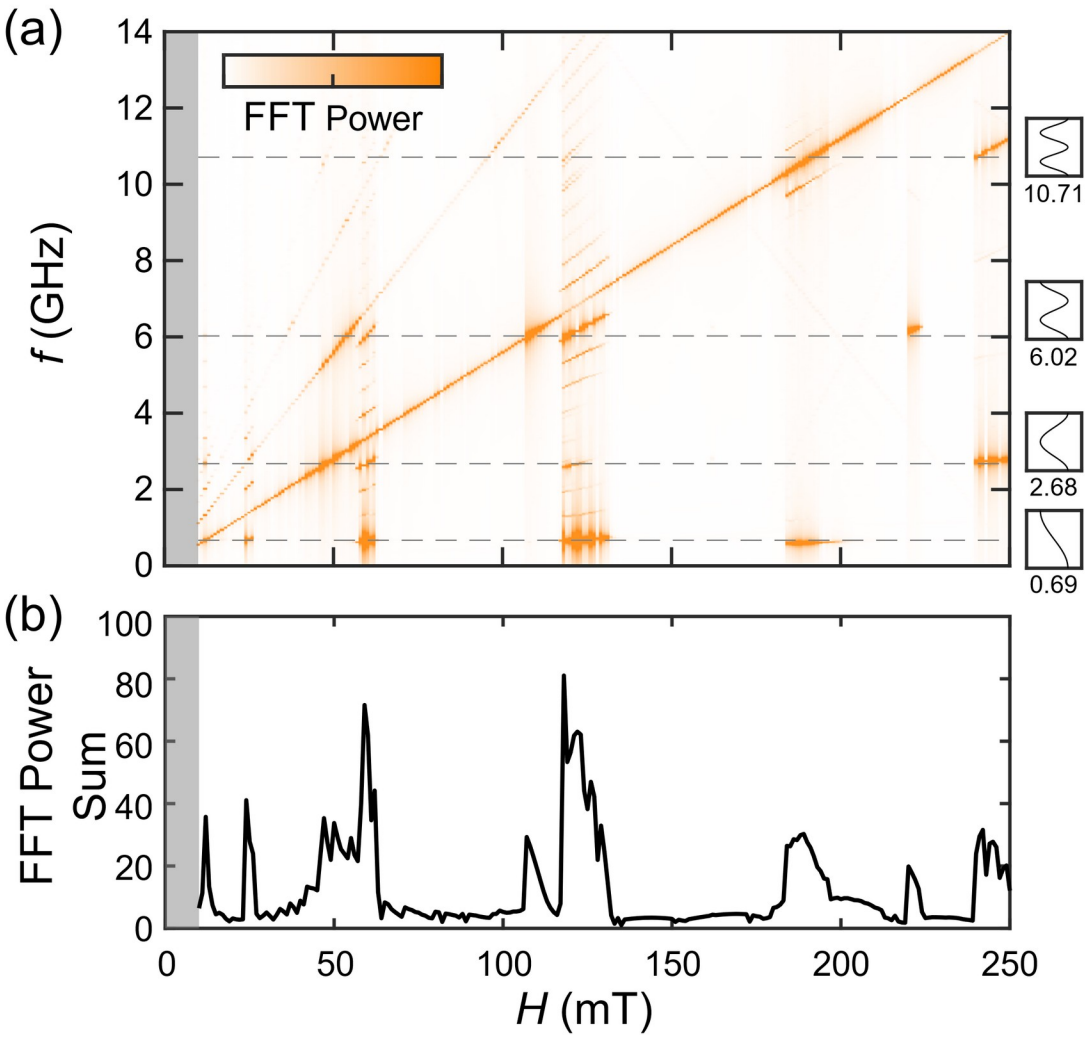
(a)
FFT Power
f (GHz)
14
12
10
8
6
4
2
0
10.71
6.02
2.68
0.69
(b)
FFT Power Sum
100
80
60
40
20
0
0
50
100
150
200
250
H (mT)

FIG. 6.

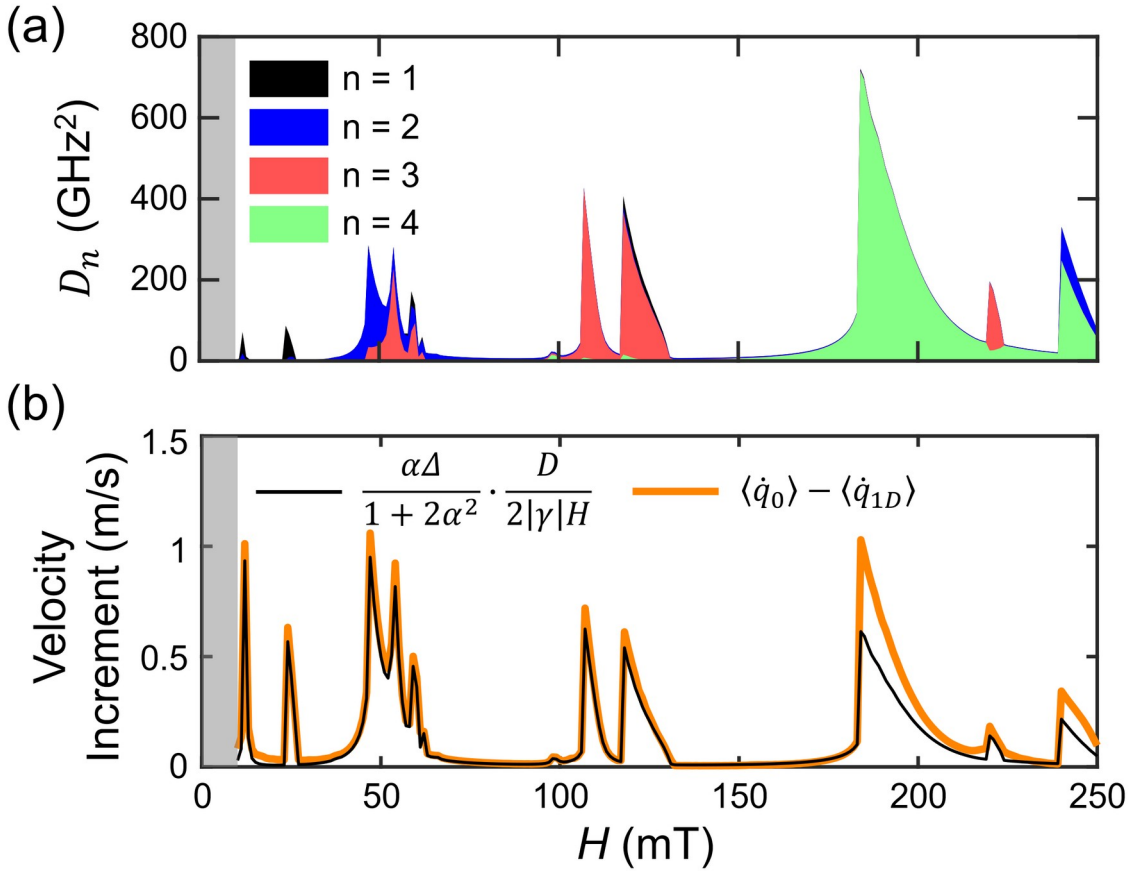
(a)
800
600
400
200
0
D_n (GHz^2)
n = 1
n = 2
n = 3
n = 4
(b)
1.5
1
0.5
0
Velocity Increment (m/s)
$\frac{\alpha\Delta}{1+2\alpha^2}\cdot\frac{D}{2|\gamma|H}$
$\langle\dot{q}_0\rangle - \langle\dot{q}_{1D}\rangle$
0
50
100
150
200
250
H (mT)
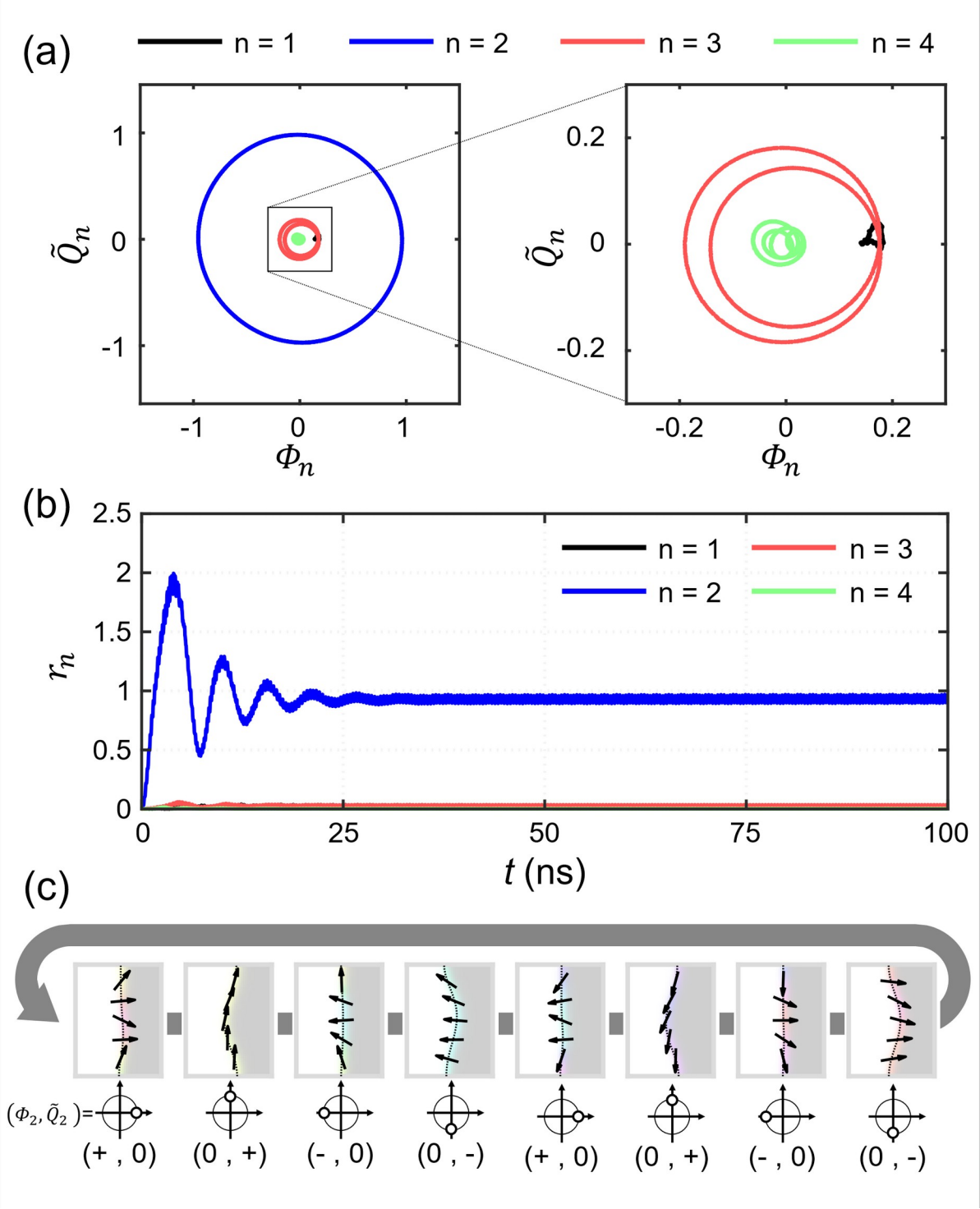
FIG. 7.